

# Understanding the Extratropical Liquid Water Path Feedback in Mixed-Phase Clouds with an Idealized Global Climate Model

Michelle Frazer<sup>1,1,1</sup> and Yi Ming<sup>2,2,2</sup>

<sup>1</sup>Princeton University

<sup>2</sup>NOAA/Geophysical Fluid Dynamics Laboratory

November 30, 2022

## Abstract

A negative shortwave cloud feedback associated with higher extratropical liquid water content in mixed-phase clouds is a common feature of global warming simulations, and multiple mechanisms have been hypothesized. A set of process-level experiments performed with an idealized global climate model show that the common picture of the liquid water path (LWP) feedback in mixed-phase clouds being controlled by the amount of ice susceptible to phase change is not robust. Dynamic condensate processes—rather than static phase partitioning—directly change with warming, with varied impacts on liquid and ice amounts. Here, three principal mechanisms are responsible for the LWP response, namely higher adiabatic cloud water content, weaker liquid-to-ice conversion through the Bergeron-Findeisen process, and faster melting of ice and snow to rain. Only melting is accompanied by a substantial loss of ice, while the adiabatic cloud water content increase gives rise to a net increase in ice water path (IWP) such that total cloud water also increases without an accompanying decrease in precipitation efficiency. Perturbed parameter experiments with a wide range of climatological LWP and IWP demonstrate a strong dependence of the LWP feedback on the climatological LWP and independence from the climatological IWP and supercooled liquid fraction. This idealized setup allows for a clean isolation of mechanisms and paints a more nuanced picture of the extratropical mixed-phase cloud water feedback than simple phase change.



## ABSTRACT

9 A negative shortwave cloud feedback associated with higher extratropical liquid water content in  
10 mixed-phase clouds is a common feature of global warming simulations, and multiple mechanisms  
11 have been hypothesized. A set of process-level experiments performed with an idealized global  
12 climate model (a dynamical core with passive water and cloud tracers and full Rotsteyn-Klein  
13 single-moment microphysics) show that the common picture of the liquid water path (LWP)  
14 feedback in mixed-phase clouds being controlled by the amount of ice susceptible to phase change  
15 is not robust. Dynamic condensate processes—rather than static phase partitioning—directly  
16 change with warming, with varied impacts on liquid and ice amounts. Here, three principal  
17 mechanisms are responsible for the LWP response, namely higher adiabatic cloud water content,  
18 weaker liquid-to-ice conversion through the Bergeron-Findeisen process, and faster melting of ice  
19 and snow to rain. Only melting is accompanied by a substantial loss of ice, while the adiabatic cloud  
20 water content increase gives rise to a net increase in ice water path (IWP) such that total cloud water  
21 also increases without an accompanying decrease in precipitation efficiency. Perturbed parameter  
22 experiments with a wide range of climatological LWP and IWP demonstrate a strong dependence  
23 of the LWP feedback on the climatological LWP and independence from the climatological IWP  
24 and supercooled liquid fraction. This idealized setup allows for a clean isolation of mechanisms  
25 and paints a more nuanced picture of the extratropical mixed-phase cloud water feedback than  
26 simple phase change.

## 27 **1. Introduction**

28 With atmospheric warming from greenhouse gases, cloud properties would vary in manifold  
29 ways, resulting in further changes in radiative fluxes and climate. Despite the recent advances  
30 in mechanistic understanding, the so-called cloud feedback is widely considered to be the largest  
31 contributor to the uncertainties in climate sensitivity and model projection of future warming  
32 (Sherwood et al. 2020). Ceppi et al. (2017) identifies three robust components of cloud feedback  
33 in comprehensive global climate models (GCMs): a positive longwave feedback from rising free  
34 tropospheric clouds, a positive shortwave (SW) feedback from decreasing subtropical low cloud  
35 fraction, and a negative SW feedback from increasing extratropical cloud optical depth.

36 Uncertainty associated with cloud feedback is dominated by the SW components (Soden and  
37 Vecchi 2011; Vial et al. 2013). Among these, this study focuses on the component that affects  
38 radiation through altering cloud optical depth or brightness (as opposed to cloud fraction). This  
39 cloud optical depth feedback is robustly negative in the Coupled Model Intercomparison Project  
40 Phase 5 (CMIP5) GCMs (Zelinka et al. 2016), though it may be artificially tuned to a small range  
41 (McCoy et al. 2016), and mechanistic uncertainty still abounds (Gettelman and Sherwood 2016;  
42 Ceppi et al. 2017; Korolev et al. 2017). Observations have shown that in pure liquid and mixed-  
43 phase (liquid and ice co-existing) clouds, cloud optical depth is primarily controlled by liquid  
44 water path (LWP), which is the vertically integrated cloud liquid (Stephens 1978). Ice affects cloud  
45 optical depth to a lesser extent owing to larger sizes of ice particles and ice water path (IWP) being  
46 generally smaller than LWP (Pruppacher and Klett 2010; McCoy et al. 2014; Cesana and Storelmo  
47 2017). GCMs predict a robust extratropical LWP increase in response to global warming, which  
48 is thought to be the main driver of the negative SW cloud feedback (e.g. Ceppi et al. 2016).

Recent modeling studies have highlighted the need to improve GCM representation of the extratropical cloud feedback. Zelinka et al. (2020) showed that the increased climate sensitivity in CMIP6 models relative to CMIP5 is largely due to changes in this feedback. The multi-model ensemble mean changes from negative in CMIP5 to slightly positive in CMIP6 presumably due to model physics differences. Therefore, it is critical to delineate the underlying mechanisms of the extratropical cloud feedback and its various components.

Multiple pathways have been proposed to explain the extratropical increase (Ceppi et al. 2017) in liquid cloud condensate. The first is an increase in the adiabatic cloud water content. With warming, the amount of water condensed in saturated updrafts increases (Tselioudis et al. 1992; Gordon and Klein 2014); the fractional change is greater at colder temperatures (Betts and Harshvardhan 1987; Somerville and Remer 1984). The second mechanism involves phase change in mixed-phase clouds (e.g., Mitchell et al. 1989; Senior and Mitchell 1993; McCoy et al. 2015; Storelvmo et al. 2015; Tan et al. 2018), which occurs only at temperatures below freezing. As isotherms shift upward with warming, the liquid-to-ice ratio at a given mixed-phase cloud location is likely to increase (Tan et al. 2016), thereby increasing cloud optical depth. An implication of this phase change mechanism is that since liquid precipitates less efficiently than ice, total cloud water content may increase (Klein et al. 2009; McCoy et al. 2015; Ceppi et al. 2016; McCoy et al. 2018). This work will address both mechanisms and their impacts on LWP and IWP. A third potential mechanism frequently mentioned in the literature is poleward jet shifts. As this effect is highly model dependent and unlikely to be dominant (Kay et al. 2014; Ceppi and Hartmann 2015; Wall and Hartmann 2015; Ceppi et al. 2016), it is not explored here.

The relative importance of the proposed mechanisms is still unclear. LWP itself is robustly linked to temperature in both models (Ceppi et al. 2016) and observations (Terai et al. 2019), hinting at the potential for emergent constraints on the negative SW cloud feedback. McCoy et al. (2016) noted

73 that among CMIP5 GCMs, T5050, the diagnosed temperature at which liquid and ice exists in  
74 equal amounts globally, is strongly anti-correlated with LWP, but positively correlated with cloud  
75 fraction despite the lack of a physical explanation. At the same time, the range of T5050 (as well as  
76 a similarly-defined 90% glaciated temperature) estimated from space-borne observations is much  
77 lower than that diagnosed from CMIP5 models, suggesting that the models tend to freeze liquid  
78 at temperatures that are too high (Cesana et al. 2015; McCoy et al. 2016). Multiple GCM studies  
79 (McCoy et al. 2014; Tan et al. 2016; Frey and Kay 2018) have shown that increasing the ratio of  
80 supercooled liquid to total water (the so-called supercooled liquid fraction or SLF) in mixed-phase  
81 clouds decreases the SW negative feedback, and thus increases climate sensitivity. These results  
82 have been attributed to models with higher T5050 having more susceptible ice (McCoy et al. 2018),  
83 which is hypothesized to control the feedback strength (as in Tan et al. 2018). Improvements in  
84 understanding the governing mechanisms are especially important as some modeling studies with  
85 observationally-based constraints have suggested that the negative SW cloud optical depth feedback  
86 is too strong or even of the wrong sign in GCMs, implying that the actual climate sensitivity may  
87 be underestimated (e.g. Tan et al. 2016; Terai et al. 2016).

88 This work utilizes an idealized model to probe the physical mechanisms underlying the extratrop-  
89 ical cloud water feedback. Idealized models complement comprehensive GCMs (Held 2005, 2014)  
90 since their workings are relatively easy to understand (Pierrehumbert et al. 2007). This is particu-  
91 larly true as previous studies of mixed-phase clouds are hindered by the non-linear complexity of  
92 cloud microphysics and the potential for unrealistic interactions between different parameterized  
93 processes (Ceppi et al. 2017). We seek to test the plausibility of the leading hypotheses in the  
94 mixed-phase cloud feedback literature including the simple conceptual picture of liquid replacing  
95 ice with warming, which has fueled the notion of the extratropical LWP feedback being controlled  
96 by the amount of susceptible ice. As mentioned above, more ice in the control climate is thought

97 to cause a greater increase in liquid with warming. The main supporting evidence is the positive  
98 correlation between the LWP feedback and climatological SLF or T5050 (McCoy et al. 2018; Tan  
99 et al. 2018). With a set of targeted, process-level experiments, we seek to explore the complexity  
100 of the mixed-phase cloud feedback. We also use a perturbed parameter ensemble of experiments  
101 with varied cloud physics settings to investigate the feasibility of predicting the LWP feedback  
102 from the control climate.

103 This paper is arranged as follows. Section 2 outlines the methodology. Section 3 presents the  
104 results from process-level and perturbed parameter experiments. Section 4 compares with previous  
105 studies with the goal of examining the plausibility of the phase change mechanism and other related  
106 arguments. Section 5 concludes as to rethinking the physical picture of the extratropical mixed-  
107 phase cloud feedback and suggests a path for future research.

## 108 **2. Methodology**

109 The idealized GCM used here combines a simple dry GCM with passive water and clouds as  
110 described in detail in Ming and Held (2018). The core is Held-Suarez dry dynamics (Held and  
111 Suarez 1994) at a T42 horizontal resolution (about  $2.8^\circ$  spacing) with 20 equally spaced vertical  
112 layers. Passive water vapor and cloud tracers (specific humidity, cloud liquid mixing ratio, cloud  
113 ice mixing ratio, and cloud fraction) are included, but are not allowed to feedback on the dynamics  
114 (i.e., no latent heating or cloud radiative effects). The cloud tracers evolve following a prognostic  
115 large-scale cloud scheme with bulk single-moment microphysics. The sub-grid-scale total-water-  
116 based relative humidity (RH) is assumed to follow a beta distribution, which is a function of the  
117 grid-mean RH. The beta distribution is designed such that a grid box with a mean total-water-based  
118 RH value above a certain threshold value ( $RH_c$ , 83.3% at the default half-width of 0.2) would  
119 have sub-grid-scale RH over 100%, thus producing clouds. The role of surface evaporation to

120 create the water vapor tracer is mimicked by nudging air parcels below 850 hPa toward saturation  
121 as in Galewsky et al. (2005). As clouds are completely decoupled from dynamics, this model is  
122 a unique tool for isolating individual mechanisms in a clean fashion without circular feedbacks.  
123 With no convective parameterization, the application of the cloud scheme is limited to stratiform  
124 clouds (and not any mixed-phase clouds formed in shallow convection). Yet, as noted in Ming  
125 and Held (2018), while idealized, this model provides strong representation of cloud distribution  
126 in the extratropical free troposphere. The control simulation (Ctrl) is the model's default climate.  
127 For Ctrl and all perturbation experiments, the atmospheric state (e.g., temperature and winds) is  
128 identical at every time step. All model simulations include a 300-day spin-up, and the next 1000  
129 days are averaged for analysis.

130 The bulk microphysics scheme has separate but interconnected treatments of liquid and ice based  
131 on Rotstajn (1997) and Rotstajn et al. (2000). The same scheme is also used in the GFDL AM2.1  
132 model, one of the two models compared in Ceppi et al. (2016). As shown in Fig. 1, water vapor forms  
133 cloud liquid and ice through condensation and deposition, respectively. The initial partitioning of  
134 cloud liquid and ice is based entirely on temperature. All condensate at temperatures greater than  
135  $-40^{\circ}\text{C}$  is formed as liquid based on the consideration that ice nuclei are generally limited in the  
136 atmosphere (Rotstajn et al. 2000). Supercooled liquid (existing between  $0^{\circ}$  and  $-40^{\circ}\text{C}$ ) can then be  
137 converted to ice principally through the Bergeron-Findeisen (BF) process (and without an explicit  
138 treatment of heterogeneous ice nucleation). In the control climate, the primary sink of water vapor  
139 (98.8% globally) is conversion to cloud liquid. Microphysical sources of water vapor come from  
140 cloud liquid (evaporation), cloud ice (ice sublimation), rain (rain evaporation), and snow (snow  
141 sublimation). Together, rain evaporation and snow sublimation, the most significant microphysical  
142 sources, comprise 22.3% of all water vapor sources. Surface evaporation (a non-microphysical  
143 source) constitutes the main supplier of water vapor (76.4%).



144 Cloud liquid forms rain through autoconversion and accretion. To facilitate conversion of cloud  
145 liquid to ice through the BF process, a minimum amount of ice crystal mass ( $10^{-12}$  kg) on which  
146 deposition can occur is assumed to be always present. (Note that the BF process is not formulated  
147 to be explicitly linked to aerosols.) Cloud liquid is also converted to cloud ice through riming  
148 (accretion of cloud liquid by ice) and homogeneous freezing (colder than  $-40^{\circ}\text{C}$ ). Overall, 68.2% of  
149 cloud liquid sinks are to rain and 30.9% to cloud ice. Cloud ice is lost almost completely (98.3%)  
150 to snow through ice settling. In the microphysics scheme, cloud ice and snow are treated effectively  
151 as one species, experiencing the same fall rate, and are only distinguished by their location in or  
152 outside of a cloud. Ice and snow can melt into rain: if this takes place in a cloud, it is considered  
153 melting of ice; if it takes places outside of a cloud, it is considered melting of snow. Cloud ice is  
154 also lost to water vapor through sublimation.

155 The *process-level experiments* involve increasing the temperature field fed to certain parts of  
156 the microphysics scheme or the formulation of surface evaporation by 2 K (summarized in Table  
157 1). These isolated warming experiments are designed after Ceppi et al. (2016). Here, in the  
158 microphysics scheme (same as that used in the AM2.1 aquaplanet in Ceppi et al. (2016)), there  
159 are at least four explicitly temperature-dependent processes: partitioning of newly formed cloud  
160 condensate, the BF process, homogeneous freezing, and melting of ice and snow. When water  
161 vapor experiences condensation/sublimation at the beginning of the microphysics scheme, it is  
162 initially partitioned into cloud liquid and ice based solely on temperature. Only liquid is created at  
163 temperatures warmer than  $-40^{\circ}\text{C}$ , and only ice otherwise. Supercooled liquid can be converted to  
164 ice through the BF process, homogeneous freezing, and riming. For the BF process, temperature  
165 affects whether or not the process occurs (below  $0^{\circ}\text{C}$ ) as well as the rate of cloud liquid being  
166 converted to cloud ice, which is greater at lower temperatures (see Eqn. A8). These two effects are  
167 tested in combination (BF2K, subjecting the *BF* process to a 2-*K* warming). (By contrast, riming

168 is not directly dependent on temperature; see Eqn. A10.) Homogeneous freezing of cloud liquid to  
169 ice occurs only when the temperature is less than  $-40^{\circ}\text{C}$  and converts all cloud liquid to ice. Ice and  
170 snow melt into rain only when the temperature is higher than  $0^{\circ}\text{C}$ , with the melting being limited  
171 to the amount that would restore the grid-box temperature to  $0^{\circ}\text{C}$ . Melting of ice and snow are  
172 tested in combination (ME2K, subjecting *melting* to a 2-K warming). All of these microphysical  
173 processes—initial partitioning, the BF process, homogeneous freezing, and melting—are also  
174 perturbed in tandem in MI2K (2-K warming of *microphysics*).

175 A significant influence of temperature in the cloud scheme is in the calculation of the saturation  
176 specific humidity ( $q_s$ ) and related variables (the  $T$  derivative of  $q_s$ , the psychrometric constant,  
177 and the sum of the vapor diffusion and thermal conductivity factors) that are used in many parts  
178 of the scheme. Since surface evaporation is also formulated in parallel based on  $q_s$ ,  $q_s$  for  
179 microphysics and surface evaporation are perturbed simultaneously in Qse2K (2-K warming of  $q_s$   
180 for the stratiform cloud scheme and *evaporation*). This experiment enables us to study the effect  
181 of the adiabatic cloud water content increase. Finally, to cover all the aforementioned effects of  
182 temperature as well as any other effects (such as the influence of temperature on air density), a 2-K  
183 temperature increase is fed to the cloud scheme and surface evaporation to create the Tse2K (full  
184 warming) experiment.

185 To develop a predictive theory of the extratropical mixed-phase cloud feedback that is applicable  
186 to a wide range of control states, a set of *perturbed parameter experiments* (also summarized in  
187 Table 1) are created by systematically modifying three key parameters of the cloud scheme. The  
188 first two have been suggested as significant for the mixed-phase cloud feedback: the strength of  
189 the BF process may be too efficient (Tan et al. 2016) and  $RH_c$  too high (McCoy et al. 2016). To  
190 vary the strength of the BF process, the formula for the conversion rate is altered arbitrarily by  
191 multiplying with a constant (0.25, 0.5, 2 or 4). The corresponding experiments are labeled as

quarBF, halvBF, doubBF and quadBF. Note that these adjustments do not result in actual changes in the BF rate as large as those imposed. The effective  $RH_c$  (83.3% in Ctrl) is varied from 76.7% to 90.0% at increments of  $\sim 3.3\%$  (rh767, rh800, rh867, and rh900) by altering the half-width of the sub-grid-scale RH beta distribution. Finally, a third parameter is chosen to cleanly affect the mean-state amount of cloud ice: the fall speed of cloud ice (relative to the large-scale vertical motion) is perturbed by multiplying with a constant (0.5, 0.75, 1.25 or 1.5). The corresponding experiments are v050, v075, v125 and v150. For each of these states, a Tse2K simulation (increasing the temperature field fed to the cloud scheme and surface evaporation by 2 K) is created, and the response (for example, rh767\_Tse2K minus rh767) analyzed.

The key to understanding the steady-state mixing ratios of cloud liquid and ice ( $q_l$  and  $q_i$ , respectively) and their responses to the warming is how they are related to the time tendencies of the aforementioned microphysical processes. To illustrate the point, let us write the time derivative of a variable  $q$  ( $q_l$  or  $q_i$ ) as:

$$\frac{dq}{dt} = s - aq^b, \quad (1)$$

where  $s$  is the source term, and the sink term is parameterized as a power-law function of  $q$  with  $a$  and  $b$  as constants. It follows that the fractional change of  $q$  can be related to the fractional change of  $s$  by:

$$\frac{\delta q}{q} = \frac{1}{b} \frac{\delta s}{s}. \quad (2)$$

The formulation and behavior of the autoconversion parameterization (Eqn. A1) are discussed in Golaz et al. (2011) (see their Equations 12-14). Although the rate is nominally proportional to  $q_l^{7/3}$ , it is effectively controlled by a numerical limiter (Eqn. A3), which tends to set  $q_l$  at a critical value ( $q_{crit}$ ) determined by a tunable threshold droplet radius ( $r_{thresh}$ ) and droplet number concentrations ( $N$ ). Since neither  $r_{thresh}$  nor  $N$  changes in this study,  $q_l$  should be close to  $q_{crit}$

213 when autoconversion is the dominant process. By contrast, accretion is proportional to  $q_l$  and the  
 214 flux of rain (Eqn. A4). The BF rate (Eqn. A8) is effectively independent of  $q_l$ , but conditionally  
 215 proportional to  $q_i^{1/3}$ . Riming (Eqn. A10) is proportional to  $q_l$  and the flux of settling ice, which is  
 216 related to the fall speed and  $q_i$ . Similarly, ice settling (Eqn. A6) at a specific level is determined  
 217 by the fall speed and vertical gradient of  $q_i$  ( $\partial q_i / \partial p$ , where  $p$  denotes pressure). If  $q_i$  is altered by  
 218 the same ratio throughout the column, an assumption that holds approximately for the simulations  
 219 examined here, the fractional change in the ice settling rate would be the same as that in  $q_i$ . The  
 220 microphysical tendency equations are listed in the Appendix for reference. Condensation and  
 221 deposition, the main sources of cloud liquid and ice, are not directly related to  $q_l$  or  $q_i$ .

222 The analysis focuses on two variables: LWP and IWP, which are, respectively, vertically inte-  
 223 grated cloud liquid and cloud ice in units of  $\text{g m}^{-2}$ . Absolute and fractional changes in LWP and  
 224 IWP are normalized by warming and thus given in units of  $\text{g m}^{-2} \text{K}^{-1}$  and  $\%$   $\text{K}^{-1}$ , respectively.  
 225 Due to the highly simplified nature of the boundary layer in this model (i.e., surface evaporation  
 226 saturating the air below 850 hPa), for the purposes of this analysis the vertical integral has a lower  
 227 boundary of 850 hPa such that LWP and IWP only represent the cloud condensate above 850 hPa.  
 228 Similarly, specific humidity and cloud condensate tendency terms, when column-integrated, only  
 229 represent values above 850 hPa.  $30^\circ$  to  $60^\circ$  and  $60^\circ$  to  $90^\circ$  are considered the mid-latitudes and  
 230 high-latitudes, respectively, and together they are considered the extratropics. Data is averaged  
 231 between the two hemispheres because of the hemispheric symmetry of the simulated climate. The  
 232 supercooled liquid fraction (SLF) is calculated as the ratio of cloud liquid to total cloud water  
 233 (liquid and ice). The daily SLF is binned as a function of temperature at an interval of 0.1 K  
 234 for each grid box in the extratropical region above 850 hPa with the temperature at which SLF is  
 235 closest to 50% considered to be T5050 (liquid and ice partitioned equally).

### 3. Results

#### *a. Process-level Experiments*

Fig. 2 shows the zonal-mean LWP and IWP (averaged between hemispheres) in the control case (Ctrl), yielding a picture of the model’s default climate [see Ming and Held (2018) for other related variables including RH and CF]. Here, LWP dominates IWP equatorward of the storm tracks (at around  $45^\circ$ ); note that this LWP/IWP ratio is not directly comparable with full GCMs as here the boundary layer is excluded in the calculation of LWP and IWP. In the total warming experiment (Tse2K), the general features, including the location of the storm tracks, remain the same. Both LWP and IWP are higher at all latitudes in the warmer climate. The increase in LWP is more pronounced than that in IWP in the mid-latitudes, while they are more comparable in the high-latitudes.

Table 2 and Fig. 3 break down the LWP and IWP feedbacks seen in Tse2K. The increase in LWP (Fig. 3a) in the extratropics is dominated by the microphysical component (MI2K) with a much smaller (slightly less than 20%) contribution from the increased  $q_s$  (Qse2K). MI2K and Qse2K combine nearly linearly to produce the full Tse2K increase in LWP suggesting that Tse2K does not add any significant temperature-affected processes beyond those perturbed in MI2K and Qse2K. The LWP feedback from the adiabatic water content increase is stronger in the high-latitudes ( $5.2\% \text{ K}^{-1}$ ) than in the mid-latitudes ( $1.6\% \text{ K}^{-1}$ ), as one would expect from the nonlinear temperature-dependence of the Clausius-Clapeyron relation.

Within the combined microphysical component, the BF process (BF2K) is responsible for most of the LWP increase, with a smaller contribution from melting (ME2K) present only in the mid-latitudes (Fig. 3b), and homogeneous freezing and initial phase partitioning producing negligible results (presumably because of the small amount of cloud condensate present near  $-40^\circ\text{C}$ ). The

BF effect is realized through the temperature-dependence of the conversion rate, as opposed to the temperature threshold at which the BF process takes control. LWP increases as the BF process slows down, converting less liquid to ice. The melting of snow to rain dominates the melting of ice to rain in terms of their effects in enhancing LWP. As discussed later, this can be conceptualized as a consequence of weaker riming since there is less snow (falling ice) to collect cloud liquid. Thus, we conclude that the increase in LWP with warming results primarily from a significant weakening of the BF process.

The IWP feedback is more nuanced. As shown in Fig. 3c, Qse2K and MI2K produce opposite effects: IWP increases at all latitudes in the former, while it decreases in the mid-latitudes with no significant change in the high-latitudes in the latter. In Qse2K, the normalized fractional increase in the high-latitude IWP ( $7.9\% \text{ K}^{-1}$ ) is greater than the mid-latitude counterpart ( $6.7\% \text{ K}^{-1}$ ), consistent with the adiabatic water content increasing with temperature at a faster rate at colder temperatures. The net result in Tse2K, to which Qse2K and MI2K add effectively linearly, is an increase in IWP, principally poleward of  $45^\circ$ . The relative importance of the BF process versus melting is reverse to the LWP feedback. The microphysical effect is dominated by ME2K (Fig. 3d); the enhanced melting of snow contributes to the lowering of IWP more than that of cloud ice. By contrast, BF2K gives rise to very little change in IWP. The fact that a weakening of the BF process causes a large increase in LWP, but no concurrent decrease in IWP is somewhat counter-intuitive, a point to which we will return later in this section when discussing the BF2K results in detail. (As with LWP, perturbing homogeneous freezing or initial phase partitioning produces no significant change in IWP.)

Fig. 4 shows the vertical structures of the changes in the mixing ratios of cloud liquid and ice. To better understand the underlying physical mechanisms, the main tendency terms driving the steady-state cloud liquid and ice are plotted in Figs. 5 and 6, respectively. No appreciable change

283 in  $q_l$  is present below the freezing line in any experiment (Fig. 4) even when there are large local  
 284 changes in cloud liquid tendencies, as is the case for condensation in Qse2K (Fig. 5a). It is also  
 285 clear from Fig. 5 that autoconversion and accretion are the principal sinks of  $q_l$  above  $0^\circ\text{C}$  in  
 286 Ctrl, with autoconversion slightly stronger. As explained in Section 2,  $q_{crit}$  exerts a strong control  
 287 over  $q_l$  when autoconversion dominates. By contrast, the BF process and riming take over in the  
 288 mixed-phase cloud temperature range (between  $0^\circ$  and  $-40^\circ\text{C}$ ). Both the BF process and riming  
 289 increase with the enhanced condensation in Qse2K (Fig. 5m and q). While the BF process is  
 290 independent of  $q_l$ , since riming is proportional to  $q_l$  steady-state  $q_l$  increases (Fig. 4a). On the ice  
 291 side, faster riming acts to increase  $q_i$  (Fig. 6e). Moreover, the increased condensation leads directly  
 292 to higher  $q_i$  through the BF process (Fig. 6a), which is conditionally proportional to  $q_i^{1/3}$ . The  
 293 resulting higher flux of settling ice, which is formulated to be approximately proportional to  $q_i$ ,  
 294 tends to further accelerate riming, but lower  $q_l$ . This cancels out much of the increase in  $q_l$  caused  
 295 by the increased condensation (Fig. 4a). The end result is that the normalized fractional increase  
 296 in the extratropical IWP ( $6.8\% \text{ K}^{-1}$ ) is much greater than the LWP counterpart ( $1.7\% \text{ K}^{-1}$ ).

297 The imposed warming to the BF process (BF2K) slows down the BF conversion from liquid  
 298 to ice (Fig. 5n). Since autoconversion and accretion play limited roles in the mixed-phase cloud  
 299 regime, an acceleration of riming (Fig. 5r) is the only way to re-establish the  $q_l$  tendency balance,  
 300 causing a significant increase in  $q_l$  (Fig. 4b). This re-balancing can be conceptualized as a weaker  
 301 BF process producing more cloud liquid to be scavenged by falling ice through riming. Since  
 302 the  $q_l$  and  $q_i$  tendencies (and their changes) are of the same magnitude but opposite signs for the  
 303 BF process and riming, the effect of the two processes on  $q_i$  is dictated by the balance of their  
 304  $q_l$  counterparts (Fig. 6b and f). Because the effects of  $q_i$  are of opposing sign, there is near-zero  
 305 net change in cloud ice (Fig. 4f). This somewhat counterintuitive result emphasizes the need to  
 306 evaluate changes in  $q_l$  and  $q_i$  based on process changes and a dynamic re-balancing of sources

307 and sinks. For example, when weakened BF process (as through warming) experiments were run  
308 with the riming process entirely removed from the microphysics scheme, instead of BF process  $q_i$   
309 tendency change being balanced principally by enhanced riming with little change in ice settling  
310 (as shown in Fig. 6f and j), without riming, the tendency change was principally balanced by  
311 significantly weakened ice settling.

312 The melting perturbation (ME2K) is unique in the sense that the resulting changes in cloud liquid  
313 and ice are of mirror image in terms of spatial structure (Fig. 4c and g). The main reason is that the  
314 melting perturbation effects are relatively confined to a narrow domain of a few degrees above the  
315 time-averaged freezing line. The warming-induced additional melting acts to increase the flux of  
316 rain and decrease the flux of settling ice simultaneously. Both factors have implications for  $q_l$ . The  
317 former tends to accelerate accretion with an effect of decreasing the  $q_l$  tendency, while the latter  
318 acts to slow down riming which increases the  $q_l$  tendency. The simulation shows a net increase of  
319  $q_l$ , suggesting that the latter factor prevails over the former. The signs of the simulated rate changes  
320 are consistent with the expectations, and they largely balance out each other (Fig. 5k and s), with  
321 a weaker contribution from autoconversion (Fig. 5g). On the ice side, the reduced supply of ice  
322 from riming is balanced entirely by lowering  $q_i$  and thus settling (Fig. 6g and k). The role of the  
323 BF process here is negligible as it is relatively ineffective at temperatures within a few degrees of  
324 0 °C.

325 This process-level analysis illustrates why the principal components of the full warming (Tse2K)  
326 simulation, namely Qse2K, BF2K, and ME2K, increase  $q_l$  and hence LWP, as summarized schemat-  
327 ically in Fig. 7. Although they all point in the same direction, the microphysical warming com-  
328 ponents (BF2K and ME2K) are a stronger contribution to the LWP feedback than the macro-  
329 physical/thermodynamic component (Qse2K). The extratropical IWP feedback stems from a broad  
330 increase in  $q_i$  from Qse2K being offset partially by a decrease near the freezing line from ME2K.



331 The results underscore that multiple processes with distinct characteristics are influential in shaping  
 332 the LWP and IWP responses, and contradict the common picture suggested in mixed-phase cloud  
 333 feedback literature of an effective trade-off between ice and liquid. Here, the dominant processes  
 334 which increase LWP with warming in mixed-phase clouds are not doing so at the expense of ice,  
 335 so the actual picture is more complicated than a (direct or indirect) replacement of ice with liquid  
 336 with warming. Liquid and ice in mixed-phase clouds are not in a static equilibrium; rather, they  
 337 exist in a dynamic balance of sources and sinks. These source and sink processes are directly  
 338 changed by warming as opposed to a simple temperature-dependent phase partitioning.

### 339 *b. Perturbed Parameter Experiments*

340 To further explore the sensitivity of the LWP and IWP feedbacks, a set of alternative control  
 341 states was created by altering three key aspects of the cloud scheme, namely the value of  $RH_c$ ,  
 342 the strength of the BF process and the fall speed of ice ( $v_{fall}$ , Eqn. A7), summarized in Table  
 343 1. As shown in Fig. 8, the first two changes produce a wide range of the climatological LWP  
 344 (approximately a factor of 2), but little variation in IWP. Lower  $RH_c$  or weaker BF process leads  
 345 to higher LWP. While these experiments are not designed to fully explain the insensitivity of IWP  
 346 to  $RH_c$  or the BF process in more detail than the previous section, the broad principle is that  
 347 steady-state values are determined by a dynamic balance of continuing phase conversion, not a  
 348 static equilibrium. And, ice changes are harder to manufacture using local processes (like the BF  
 349 process) when ice is so strongly controlled by gravitational settling. In the  $v_{fall}$  perturbations,  
 350 IWP varies widely (a factor of more than 3) with higher fall speed giving rise to lower IWP but  
 351 with little spread in the climatological LWP.

352 All of these perturbed parameter experiments are subjected to 2-K warming in a way analogous  
 353 to Tse2K. The resulting normalized LWP and IWP changes ( $\delta LWP$  and  $\delta IWP$ , respectively) are

354 plotted against their climatological counterparts in Fig. 9. Ranging from 2.6 to 3.4 g m<sup>-2</sup> K<sup>-1</sup>,  
 355 relative to 3.0 g m<sup>-2</sup> K<sup>-1</sup> in Tse2K (Table 2), the LWP feedback is positively correlated with the  
 356 climatological LWP (Fig. 9a). The best linear fit yields that  $\delta\text{LWP} = 0.045 \text{ LWP} + 1.60$ , with an  $R^2$   
 357 of 0.98. Thus, the fractional change can be written as  $\delta\text{LWP}/\text{LWP} = 0.045 + 1.60/\text{LWP}$ , suggesting  
 358 that the marginal gain decreases with increasing LWP. Since the four experiments targeting the BF  
 359 process, namely {quar, halv, doub, quad}BF, effectively demonstrate the basic behavior of the LWP  
 360 feedback, we start by focusing on them in the effort to explain the latter. As shown above, the main  
 361 sink terms for cloud liquid in the mixed-phase regime are the BF process and riming. As the BF  
 362 process becomes stronger from quarBF to quadBF, riming has to weaken if the total sink is constant,  
 363 giving rise to lower climatological LWP, in line with the model simulations. Recall that the riming  
 364 rate is proportional to cloud liquid. The process-level experiments suggest that the warming effect  
 365 is realized mostly through the BF process. In these experiments, the warming-induced perturbation  
 366 to the BF process is roughly proportional to its baseline rate (not shown). Therefore, the lower  
 367 the climatological LWP is, the stronger the baseline BF rate and associated perturbation are. The  
 368 combination translates into higher fractional change in LWP with lower climatological LWP (from  
 369 a stronger BF process).

370 Lowering  $RH_c$  tends to increase LWP by enhancing condensation in a way similar to Qse2K.  
 371 They differ in that the former causes a large increase in autoconversion, but without any substantial  
 372 change in accretion or riming, while all three processes increase in the latter. As explained  
 373 before, autoconversion can adjust to forced changes such as those resulting from warming without  
 374 perturbing cloud liquid. As a result, a control state with enhanced autoconversion should be less  
 375 sensitive to warming (in this limited context; other feedbacks in complex models such as that  
 376 noted in Mülmenstädt et al. (2021) may complicate this picture). This explains why lowering  $RH_c$   
 377 gives rise to larger LWP, but smaller fractional increases in response to warming. Of interest is

the minimal effect on the extratropical climatological LWP and  $\delta$ LWP from drastically changing the climatological IWP (or susceptible ice) in the ice fall speed experiments. Clearly, the LWP feedback is correlated with the climatological LWP, but not the climatological IWP. The preceding analysis also holds when the LWP feedback is further divided into the mid- and high-latitude components (not shown).

The IWP feedback is correlated strongly with the climatological IWP (Fig. 9b). Note that the variation in the IWP feedback is almost exclusively from the ice fall speed experiments (ranging from 0.57 to 1.70 g m<sup>-2</sup> K<sup>-1</sup>). An inspection of the best linear fit result ( $\delta$ IWP = 0.023·IWP + 0.031, with an  $R^2$  of 1.00) indicates that the intercept is so small that the warming-induced change in IWP is effectively proportional to the climatological IWP. In other words, the normalized fractional change is constant at 2.3% K<sup>-1</sup>. This relatively simple relation reflects the fact that gravitational settling is the main process through which cloud ice can be adjusted to re-establish the mass balance. As seen both from the process-level experiments and the BF-series parameter perturbation experiments, the amount of cloud ice is not sensitive to the BF process. In the meantime, riming is under the strong control of the cloud liquid balance. This leaves gravitational settling as the only way to alter cloud ice without affecting other processes substantially. Note that similar linear relationships hold if the climatological LWP and IWP are computed only for the mixed-phase temperature range (between 0 and -40°C), confirming the independence of the LWP feedback from the climatological IWP (or susceptible ice).

#### 4. Discussion

As noted in the introduction, much of the existing literature on the extratropical mixed-phase cloud feedback centers on the correlation between the climatological SLF/T5050 and LWP feedback. Specifically, the lower SLF is or the higher T5050 is, the stronger the LWP feedback is (Tan et al.

2016; Frey and Kay 2018; McCoy et al. 2018). The presumption is that the phase change mechanism plays a crucial role, meaning that ice would be statistically replaced by liquid as isotherms shift with warming. Thus, the climatological susceptible ice or IWP is thought to be predictive of the feedback strength, forming the basis of potential emergent constraints (Tan et al. 2016). A related argument is that the phase change would give rise to a decrease in precipitation efficiency and a net increase in total water path (TWP, the sum of LWP and IWP) as liquid is less efficient than ice in forming precipitation (McCoy et al. 2018). While it is clear from the previous section that the mixed-phase cloud feedback is much more complicated than simple phase change, we further test the validity of both claims—SLF/T5050 as a predictor and decreased precipitation efficiency increasing TWP—against our results.

The range of climatological T5050 in the perturbed parameter experiments is shown in Fig. 10: stronger BF process and higher  $RH_c$  favor lower LWP (or SLF) and higher T5050. The normalized  $\delta LWP$ , however, is strongly anti-correlated with T5050 ( $R^2 = 0.92$ , Fig. 10) as it is positively correlated with the climatological LWP (Fig. 9a). The T5050/ $\delta LWP$  anti-correlation is opposite to that expected if susceptible ice drove the LWP feedback and is contrary to the findings of Tan et al. (2016) and Frey and Kay (2018) based on the CAM5 model and of McCoy et al. (2018) based on CMIP5 models. Furthermore, as shown in Fig. 8, the climatological IWP is effectively constant for these experiments. This calls into question the hypothesis that susceptible ice controls the strength of the LWP feedback. As another evidence against the hypothesis, if the  $v_{fall}$  perturbations are included, the predictive power of T5050 is significantly diminished ( $R^2 = 0.76$ , Fig. 10). The large variations in the climatological IWP, which drive the spread in T5050 in the  $v_{fall}$  perturbations, do not affect  $\delta LWP$  significantly. Thus, any connection here between T5050 and the LWP feedback is not derived from the climatological ice but rather the climatological liquid. This finding suggests that it is important to, when showing correlation between changes in T5050 (or SLF) and LWP

feedback or climate sensitivity, also consider the independent roles of changes in climatological liquid or ice as potentially meaningful in addition to their ratio.

To understand why a T5050/LWP feedback connection might be present in some models but not others, we consider the dissection of mechanisms for LWP increase in aquaplanet versions of CAM5 and AM2.1 in Ceppi et al. (2016). AM2.1 uses virtually the same large-scale cloud parameterizations as our idealized model, and the AM2.1 results documented in Ceppi et al. (2016) are in excellent agreement with ours despite numerous differences in model setup and experimental design, a testament to the central role of cloud parameterizations in determining the feedback. Whereas both CAM5 and AM2.1 yield higher LWP in response to warming, their IWP changes differ in sign (see their Figure 2). IWP decreases in CAM5, but increases in AM2.1. Moreover, microphysical processes, especially the BF process, are responsible for the majority of the LWP increases, but cannot even account for the signs of the combined extratropical IWP changes (their Figure 7): the microphysically-induced IWP change is an increase in CAM5 and a decrease in AM2.1. Note that CAM5 implements the Morrison-Gottelman microphysics scheme (Morrison and Gottelman 2008), which differs significantly from the Rotstayn-Klein microphysics scheme (Rotstayn 1997) used in AM2.1 and our model, particularly in the treatment of ice and snow. As noted previously, the Rotstayn-Klein scheme treats cloud ice and snow indistinguishably and therefore lacks direct representation of cloud ice autoconversion and accretion by snow (though tuning of the ice fall speed can indirectly account for these sinks of cloud ice). Additionally, the Morrison-Gottelman scheme includes a representation of ice nucleation, which was found in Tan and Storelvmo (2016) to have an even stronger effect than ice fall speed on LWP and IWP. Similarly, by using the BF process to principally partition liquid and ice between 0°C and -40°C, the Rotstayn-Klein scheme does not directly account for increasingly recognized efficient ice nuclei (Kanji et al. 2017). In this sense, it is not inconceivable to see microphysically-induced IWP changes being

qualitatively different between the two models. Clearly, the large discrepancy in IWP response to warming merits further analysis and evaluation of both microphysics schemes, especially given the important role of ice cloud microphysics for Arctic cloud feedback (Tan and Storelvmo 2019).

Beyond the microphysical feedback, in the Ceppi et al. (2016) study, if one assumes linear additivity (which appears to hold) the non-microphysical component of the IWP change would be a net loss in CAM5 and a net gain in AM2.1. Our results demonstrate that the non-microphysical enhancement of IWP in AM2.1 is attributable to the adiabatic cloud water content increase, a possibility noted in Ceppi et al. (2016). Thus, attempting to reconcile this work with others raises the intriguing question of what factors could outweigh the adiabatic cloud water content effect (however strong it is) and cause the net loss seen in CAM5. These factors (perhaps related to convective ice) should be further explored in complex GCMs and the adiabatic ice effect evaluated for robustness. From the process dissection in Ceppi et al. (2016), it appears that the considerable loss of cloud ice in the warming experiments conducted with CAM5 in Tan et al. (2016) and Frey and Kay (2018) is not microphysical (stratiform) in origin, and thus should not be interpreted as being related to the concurrent increase of cloud liquid, which roots in microphysics. This mechanistic understanding casts further doubt on the susceptible ice hypothesis and other related arguments. From a broader perspective, Ceppi et al. (2016) also noted a robust extratropical LWP increase with warming in the CMIP5 model ensemble mean, without a compensating large decrease in IWP. This is consistent with other studies showing diverse extratropical LWP and IWP feedbacks in models beyond the two highlighted by Ceppi et al. (2016). For example, Lohmann and Neubauer (2018), using ECHAM6-HAM2 with microphysics after Lohmann and Roeckner (1996), found no increase in ECS with increased SLF (unlike the relation found in Tan et al. 2016). McCoy et al. (2021) showed that among CMIP5 and CMIP6 GCMs, most show an increase in liquid along with a slight reduction in ice.

Having seen no evidence of the utility of SLF/T5050 as a predictor here for LWP feedback, we  
 now consider whether decreased precipitation efficiency contributes here to the increase in TWP.  
 We calculate the large-scale precipitation efficiency as defined in Zhao (2014), which is the ratio  
 of the total cloud condensation rate (the sum of condensation and deposition fluxes) to surface  
 precipitation and represents the fraction of the condensate that subsequently rains out. There is a  
 slight increase in precipitation efficiency with warming (80.5% in Ctrl versus 81.1% in Tse2K).  
 This results from microphysical increases (80.7% in BF2K and 80.8% in ME2K) being offset by a  
 macrophysical decrease (80.0% in Qse2K). All changes are on the order of 1% or less. Critically,  
 no evidence of an increase in cloud lifetime is present, with precipitation efficiency increasing  
 rather than decreasing. Another measure of a precipitation efficiency effect is surface precipitation  
 normalized by TWP ( $P/TWP$ ) as in McCoy et al. (2015), which can be thought of as the inverse  
 of the cloud water residence time. Following the Clausius-Clapeyron relation, the extratropical  
 surface precipitation increases by  $6.9\% \text{ K}^{-1}$  in Tse2K and Qse2K, but remains essentially constant  
 in the microphysical experiments.  $P/TWP$  increases by 1.9% from  $1.03 \text{ hr}^{-1}$  in Ctrl to  $1.05 \text{ hr}^{-1}$   
 in Tse2K. Again, the net result is a slight decrease in the cloud water residence time or a slight  
 increase in precipitation efficiency. These results do not support a precipitation efficiency effect  
 with warming here as widely claimed (e.g., at the heart of the argument of Bjordal et al. 2020).

This finding does not mean a precipitation efficiency feedback is not present in reality, but it  
 may not be present in models as assumed. Mülmenstädt et al. (2021) showed that when warm rain  
 parameterizations are adjusted to better simulate reality in a complex GCM (ECHAM-HAMMOZ),  
 a large negative cloud lifetime effect becomes present. Here we show that other mechanisms can  
 explain a significant increase in LWP and TWP, emphasizing the need to carefully diagnose  
 mechanisms to explain model results which may not contain a significant precipitation efficiency  
 feedback without a warm rain efficiency adjustment. In our model, the weakening of the BF process

(BF2K) increases TWP while keeping precipitation nearly constant, suggesting that the BF process alone could affect precipitation efficiency, and thus should be the focus of research to improve its representation in models in addition to the need for improvement in warm rain efficiency as highlighted by Mülmenstädt et al. (2021)

Here, in the absence of a precipitation efficiency-mediated strong phase change effect, the adiabatic cloud water content effect is shown to be responsible for increasing TWP by enhancing both liquid and ice. McCoy et al. (2015) observed that increasing TWP was a significant contribution to increased extratropical LWP in CMIP5 models, with 20–80% of the LWP increase being due to phase re-partitioning. Using observations and modeling, McCoy et al. (2019) highlighted the primacy of the adiabatic cloud water content effect in explaining the increase in LWP with warming in extratropical cyclones. It was found that more than 80% of the enhanced Southern Ocean extratropical cyclone LWP in GCMs from warming can be predicted based on the relationship between the climatological warm conveyor belt moisture flux and cyclone LWP and the change in moisture flux with warming (see also McCoy et al. 2020). While phase change may play a role in the remaining unexplained LWP increases, especially in the poleward half of cyclones, it is clearly a secondary mechanism. A ground-based observational study (Terai et al. 2019) found that both the moist adiabatic scaling and phase partitioning mechanisms are equally important for explaining the increase in LWP with warming at cold temperatures. A complementary space-based observational study (Tan et al. 2019), however, suggests phase change is more important than the adiabatic cloud water content increase in explaining the increase in cloud optical depth with cloud top temperature. Between these observational studies, the GCM studies referenced in this Discussion section, and the idealized modeling results presented herein, it is clear that more research is clearly needed for elucidating the relative importance of the two mechanisms. These mechanisms, as well as a



520 potential precipitation efficiency mediated effect, should be carefully diagnosed in future GCM  
521 research as an important step in constraining the mixed-phase cloud feedback.

## 522 **5. Conclusions**

523 This study used an idealized GCM to perform a set of process-level experiments which delin-  
524 eated three key mechanisms of the extratropical LWP feedback involving mixed-phase clouds:  
525 higher adiabatic cloud water content, weaker liquid-to-ice conversion through the BF process, and  
526 strengthened melting of ice and snow to rain with associated impacts on riming. Over half of  
527 the extratropical LWP increase can be attributed to the weakening of the BF process, without a  
528 corresponding decrease in IWP. The extratropical IWP in fact increases with warming due to the  
529 adiabatic cloud water effect, with a small offset caused by stronger melting. Warming experiments  
530 in a perturbed parameter ensemble demonstrate a strong dependence of the LWP feedback on the  
531 climatological LWP and independence from the climatological IWP. T5050 is anti-correlated with  
532  $\delta\text{LWP}$  and is therefore only useful as a predictor insofar as it represents the climatological LWP as  
533 opposed to the climatological IWP. No associated decrease in precipitation efficiency is found in  
534 this modelling setup.

535 The overarching goal of this study is to improve mechanistic understanding of the extratropical  
536 mixed-phase cloud feedback. Our results help refine the current physical conceptualization of the  
537 LWP feedback as more nuanced than simple phase change, involving impacts of higher adiabatic  
538 cloud water content, weaker cloud liquid sinks such as the BF process, and indirect phase changes  
539 moderated by precipitation processes (especially riming). Liquid and ice in mixed-phase clouds  
540 are in a dynamic equilibrium with microphysical process efficiencies defining time-averaged phase  
541 partitioning and its change with warming. These results are helpful for guiding efforts to constrain  
542 mixed-phase parameterizations in GCMs through process-oriented diagnostics. In particular, the

543 effect of warming on the BF process, which is at the heart of mixed-phase cloud microphysics,  
544 should be better understood and represented in GCMs (see Tan and Storelvmo 2016). In addition  
545 to the BF process, the climatological LWP needs to be better constrained. Not only is it shown here  
546 to be predictive of the LWP feedback, but also the radiative impact of increases in LWP is highly  
547 dependent on the control state (Bodas-Salcedo et al. 2016, 2019). Finally, similar process-based  
548 studies among varying microphysics schemes (including those with more comprehensive treatments  
549 of cloud ice and ice nucleation) are vital, as cloud water source and sink efficiencies define the  
550 mixed-phase cloud phase partitioning (Ceppi et al. 2016). Mixed-phase cloud studies should show  
551 results at the process level to better conclude as to the driving mechanisms and implications for  
552 climate sensitivity. Because of complex interactions in full GCMs when mixed-phase physics are  
553 perturbed (as in Tan et al. 2016; Frey and Kay 2018), idealized setups such as that utilized here  
554 present a clean, complementary approach for elucidating causal relationships.

555 *Acknowledgments.* The authors acknowledge Nadir Jeevanjee, David Paynter, and three anony-  
556 mous reviewers for helpful feedback and Daniel McCoy for useful discussion. M.E.F. was supported  
557 by award NA18OAR4320123 from the National Oceanic and Atmospheric Administration, U.S.  
558 Department of Commerce, and award AWD1005319 from the National Science Foundation.

559 *Data availability statement.* The output from the simulations described in this manuscript is  
560 archived at the Geophysical Fluid Dynamics Laboratory and is available upon request.

## 561 APPENDIX

### 562 **Microphysical Transformation Equations**

563 The following equations are those parameterized in the microphysical scheme used herein (after  
564 Rotstayn 1997; Rotstayn et al. 2000).

565 *a. Precipitation Formation Processes*

566 *Autoconversion*: the time rate change of grid mean liquid from autoconversion is parameterized

567 as:

$$\left. \frac{\partial q_l}{\partial t} \right|_{au} = -q_a \times \left( \frac{0.104 g \rho^{4/3} E_{c,au}}{\mu (N \rho_l)^{1/3}} \right) \times (q_l/q_a)^{7/3} \times H(r_d - r_d^{au}) \quad (A1)$$

568 where  $\mu$  is the dynamic viscosity of air,  $E_{c,au}$  is the mean collection efficiency of the autoconversion

569 process,  $\rho_l$  is the density of pure liquid, and  $N$  is the number of cloud droplets per unit volume. In

570 the Heaviside function,  $H$ ,  $r_d^{au}$  is a critical drop radius that the mean volume radius of cloud drops,

571  $r_d$ , must exceed for autoconversion to occur, where:

$$\rho q_l / q_a = 4\pi N \rho_l r_d^3 / 3 \quad (A2)$$

572 Autoconversion is limited to that which would decrease  $q_l$  to the threshold:

$$MAX \left( - \left. \frac{\partial q_l}{\partial t} \right|_{au} \right) = \ln \left( \frac{\rho q_l / q_a}{4\pi N \rho_l (r_d^{au})^3 / 3} \right) \times \frac{q_l}{\Delta t_{cld}} \quad (A3)$$

573 *Accretion*: the time rate change of grid mean liquid from accretion is parameterized as:

$$\left. \frac{\partial q_l}{\partial t} \right|_{acc} = -a_{rain}^{cld} \times 65.8 E_{c,acc} (R_{rain}^{cld} / \rho_l a_{rain}^{cld})^{7/9} \times (q_l / q_a) \quad (A4)$$

574 where  $R_{rain}^{cld}$  is the grid mean flux of rain entering the rid box from above that enters saturated air,

575  $a_{rain}^{cld}$  is the portion of the grid box that this occurs in, and  $E_{c,acc}$  is the collection efficiency between

576 rain drops and cloud droplets which is parameterized as:

$$E_{c,acc} = r_d^2 / (r_d^2 + 20.5 \mu^2) \quad (A5)$$

577 *Gravitational Settling*: the sink of cloud ice due to gravitation settling is:

$$\left. \frac{\partial q_i}{\partial t} \right|_{gr} = - \frac{\partial}{\partial p} \{ q_a \times \rho g V_f \times (q_i / q_a) \} \quad (A6)$$

where  $V_f$  is the fall speed the cloud ice fall as relative to the large-scale vertical motion and is parameterized as:

$$V_f = 3.29(\rho q_i/q_a)^{0.16} \quad (A7)$$

#### b. Conversions between Liquid and Ice

**BF Process:** the time rate change of the Bergeron-Findeisen process (growth of an ice crystal from preferential condensation) is parameterized as:

$$\left. \frac{\partial q_l}{\partial t} \right|_{berg} = - \frac{q_a \times (N_i/\rho)^{2/3} \times 7.8 \times (MAX(q_i/q_a, M_{i0}N_i/\rho))^{1/3}}{(\rho_i)^{2/3} \times (A + B)} \quad (A8)$$

where  $N_i$  is the number of ice nuclei per unit volume,  $M_{i0}$  is the mass ( $10^{-12}$ ) of an initial crystal assumed to always be present,  $\rho_i$  is the mass density of pristine ice crystals. Additionally,  $A = (L_v/K_a T) \cdot ((L_v/R_v T) - 1)$  and  $B = R_v T / \chi e_s$ , where  $K_a$  is the thermal conductivity of air,  $\chi$  is the diffusivity of water vapor in air, and  $R_v$  is the gas constant for water vapor. The ice nuclei density,  $N_i$ , is parameterized assuming the air is a liquid water saturation:

$$N_i = 1000 \exp \left[ 12.96 \frac{(e_{sl} - e_{si})}{e_{si}} - 0.639 \right] \quad (A9)$$

where  $e_{sl}$  and  $e_{si}$  are the saturation vapor pressures over liquid and ice, respectively.

**Riming:** the time rate change of riming (falling ice colliding and coalescing with cloud droplets) is parameterized as:

$$\left. \frac{\partial q_l}{\partial t} \right|_{rim} = -a_{snow}^{cld} \times \lambda_f E_{c,rim} (R_{snow}^{cld} / 2\rho_i a_{snow}^{cld}) \times (q_l/q_a) \quad (A10)$$

where  $\rho_i$  is the assumed density of falling ice crystals,  $R_{snow}^{cld}$  is the grid mean flux of settling ice entering the rid box from above that enters saturated air,  $a_{snow}^{cld}$  is the portion of the grid box that this occurs in,  $E_{c,rim}$  is the collection efficiency for the riming process (fixed), and  $\lambda_f$  is parameterized as a function of temperature:

$$\lambda_f = 1.6 \times 10^3 \cdot 10^{0.023(276.16K - T)} \quad (A11)$$

## References

- Betts, A. K., and Harshvardhan, 1987: Thermodynamic constraint on the cloud liquid water feedback in climate models. *J. Geophys. Res.*, **92**, 8483–8485, doi:10.1029/JD092iD07p08483.
- Bjordal, J., T. Storelvmo, K. Alterskjær, and T. Carlsen, 2020: Equilibrium climate sensitivity above 5°C plausible due to state-dependent cloud feedback. *Nat. Geosci.*, **23**, 718–721, doi:10.1038/s41561-020-00649-1.
- Bodas-Salcedo, A., P. G. Hill, K. Furtado, K. D. Williams, P. R. Field, J. C. Manners, P. Hyder, and S. Kato, 2016: Large contribution of supercooled liquid clouds to the solar radiation budget of the Southern Ocean. *J. Climate*, **29**, 4213–4228, doi:10.1175/JCLI-D-15-0564.1.
- Bodas-Salcedo, A., J. P. Mulcahy, T. Andrews, K. D. Williams, M. A. Ringer, P. R. Field, and G. S. Elsaesser, 2019: Strong dependence of atmospheric feedbacks on mixed-phase microphysics and aerosol-cloud interactions in HadGEM3. *J. Adv. Model. Earth Syst.*, **11**, 1735–1758, doi:10.1029/2019MS001688.
- Ceppi, P., F. Brient, M. D. Zelinka, and D. L. Hartmann, 2017: Cloud feedback mechanisms and their representation in global climate models. *WIREs Clim. Change*, **8**, doi:10.1002/wcc.465.
- Ceppi, P., and D. L. Hartmann, 2015: Connections between clouds, radiation, and midlatitude dynamics: A review. *Curr. Clim. Change. Rep.*, **1**, 94–102, doi:10.1007/s40641-015-0010-x.
- Ceppi, P., D. L. Hartmann, and M. J. Webb, 2016: Mechanisms of the negative shortwave cloud feedback in middle to high latitudes. *J. Climate*, **29**, 139–157, doi:10.1175/JCLI-D-15-0327.1.
- Cesana, G., and T. Storelvmo, 2017: Improving climate projections by understanding how cloud phase affects radiation. *J. Geophys. Res. Atmos.*, **122**, 4594–4599, doi:10.1002/2017JD026927.

616 Cesana, G., D. E. Waliser, X. Jiang, and J. F. Li, 2015: Multimodel evaluation of cloud phase  
617 transition using satellite and reanalysis data. *J. Geophys. Res. Atmos.*, **120**, 7871–7892, doi:  
618 10.1002/2014JD022932.

619 Frey, W. R., and J. E. Kay, 2018: The influence of extratropical cloud phase and amount feedbacks  
620 on climate sensitivity. *Climate Dyn.*, **50**, 3097–3116, doi:10.1007/s00382-017-3796-5.

621 Galewsky, J., A. Sobel, and I. M. Held, 2005: Diagnosis of subtropical humidity dynamics using  
622 tracers of last saturation. *J. Atmos. Sci.*, **62**, 3353–3367, doi:10.1175/JAS3533.1.

623 Gettelman, A., and S. C. Sherwood, 2016: Processes responsible for cloud feedback. *Curr. Clim.*  
624 *Change Rep.*, **2**, 179–189, doi:10.1007/s40641-016-0052-8.

625 Golaz, J. C., M. Salzmann, L. J. Donner, L. W. Horowitz, Y. Ming, and M. Zhao, 2011:  
626 Sensitivity of the aerosol indirect effect to subgrid variability in the cloud parameterization  
627 of the GFDL atmosphere general circulation model AM3. *J. Climate*, **24**, 3145–3160, doi:  
628 10.1175/2010JCLI3945.1.

629 Gordon, N. D., and S. A. Klein, 2014: Low-cloud optical depth feedback in climate models. *J.*  
630 *Geophys. Res. Atmos.*, **119**, 6052–6065, doi:10.1002/2013JD021052.

631 Held, I. M., 2005: The gap between simulation and understanding in climate modeling. *Bull. Amer.*  
632 *Meteor. Soc.*, **86**, 1609–1614, doi:10.1175/BAMS-86-11-1609.

633 Held, I. M., 2014: Simplicity amid complexity. *Science*, **343**, 1206–1207, doi:10.1126/science.  
634 1248447.

635 Held, I. M., and M. J. Suarez, 1994: A proposal for the intercomparison of the dynamical  
636 cores of atmospheric general circulation models. *Bull. Amer. Meteor. Soc.*, **75**, 1825–1830,  
637 doi:10.1175/1520-0477(1994)075<1825:APFTIO>2.0.CO;2.

638 Kanji, Z. A., L. A. Ladino, H. Wex, Y. Boose, M. Burkert-Kohn, D. J. Cziczo, and  
 639 M. Krämer, 2017: Overview of ice nucleating particles. *Meteor. Monogr.*, **58**, 1.1–1.33, doi:  
 640 10.1175/AMSMONOGRAPHS-D-16-0006.1.

641 Kay, J. E., B. Medeiros, Y.-T. Hwang, A. Gettelman, J. Perket, and M. G. Flanner, 2014: Processes  
 642 controlling Southern Ocean shortwave climate feedbacks in CESM. *Geophys. Res. Lett.*, **41**,  
 643 616–622, doi:10.1002/2013GL058315.

644 Klein, S. A., and Coauthors, 2009: Intercomparison of model simulations of mixed-phase clouds  
 645 observed during the ARM Mixed-Phase Arctic Cloud Experiment. I: Single-layer cloud. *Quart.*  
 646 *J. Roy. Meteor. Soc.*, **135**, 979–1002, doi:10.1002/qj.416.

647 Korolev, A., and Coauthors, 2017: Mixed-phase clouds: Progress and challenges. *Meteor. Monogr.*,  
 648 **58**, 5.1–5.50, doi:10.1175/AMSMONOGRAPHS-D-17-0001.1.

649 Lohmann, U., and D. Neubauer, 2018: The importance of mixed-phase and ice clouds for climate  
 650 sensitivity in the global aerosol–climate model ECHAM6-HAM2. *Atmos. Chem. Phys.*, **18**,  
 651 8807–8828, doi:10.5194/acp-18-8807-2018.

652 Lohmann, U., and E. Roeckner, 1996: Design and performance of a new cloud microphysics  
 653 scheme developed for the ECHAM general circulation model. *Climate Dyn.*, **12**, 557–572,  
 654 doi:10.1007/BF00207939.

655 McCoy, D. T., P. Field, A. Bodas-Salcedo, G. S. Elsaesser, and M. D. Zelinka, 2020: A regime-  
 656 oriented approach to observationally constraining extratropical shortwave cloud feedbacks. *J.*  
 657 *Climate*, **33**, 9967–9983, doi:10.1175/JCLI-D-19-0987.1.

658 McCoy, D. T., D. L. Hartmann, and D. P. Grosvenor, 2014: Observed Southern Ocean cloud prop-  
659 erties and shortwave reflection. Part I: Calculation of SW flux from observed cloud properties.  
660 *J. Climate*, **27**, 8836–8857, doi:10.1175/JCLI-D-14-00287.1.

661 McCoy, D. T., D. L. Hartmann, and M. D. Zelinka, 2018: Mixed-phase cloud feedbacks. *Mixed-  
662 Phase Clouds: Observations and Modeling*, C. Andronache, Ed., Elsevier, 215–236, doi:10.  
663 1016/B978-0-12-810549-8.00009-X.

664 McCoy, D. T., D. L. Hartmann, M. D. Zelinka, P. Ceppi, and D. P. Grosvenor, 2015: Mixed-phase  
665 cloud physics and Southern Ocean cloud feedback in climate models. *J. Geophys. Res. Atmos.*,  
666 **120**, 9539–9554, doi:10.1002/2015JD023603.

667 McCoy, D. T., I. Tan, D. L. Hartmann, M. D. Zelinka, and T. Storelvmo, 2016: On the relationships  
668 among cloud cover, mixed-phase partitioning, and planetary albedo in GCMs. *J. Adv. Model.  
669 Earth Syst.*, **8**, 650–668, doi:10.1002/2015MS000589.

670 McCoy, D. T., and Coauthors, 2019: Cloud feedbacks in extratropical cyclones: insight from long-  
671 term satellite data and high-resolution global simulations. *Atmos. Chem. Phys.*, **19**, 1147–1172,  
672 doi:10.5194/acp-19-1147-2019.

673 McCoy, D. T., and Coauthors, 2021: Extratropical shortwave cloud feedbacks in the context of the  
674 global circulation and hydrological cycle. *under review in GRL*.

675 Ming, Y., and I. M. Held, 2018: Modeling water vapor and clouds as passive tracers in an idealized  
676 GCM. *J. Climate*, **31**, 775–786, doi:10.1175/JCLI-D-16-0812.1.

677 Mitchell, J., C. Senior, and W. Ingram, 1989: CO<sub>2</sub> and climate: a missing feedback? *Nature*, **341**,  
678 132–134, doi:10.1038/341132a0.



679 Morrison, H., and A. Gettelman, 2008: A new two-moment bulk stratiform cloud microphysics  
680 scheme in the Community Atmosphere Model, version 3 (CAM3). Part I: Description and  
681 numerical tests. *J. Climate*, **21**, 3642–3659, doi:10.1175/2008JCLI2105.1.

682 Mülmenstädt, J., and Coauthors, 2021: An underestimated negative cloud feedback from cloud  
683 lifetime changes. *Nat. Clim. Change*, **11**, 508–513, doi:10.1038/s41558-021-01038-1.

684 Pierrehumbert, R. T., H. Brogniez, and R. Roca, 2007: On the relative humidity of the atmosphere.  
685 *The Global Circulation of the Atmosphere*, T. Schneider, and A. H. Sobel, Eds., Princeton  
686 University Press, 143–185.

687 Pruppacher, H., and J. Klett, 2010: Cloud chemistry. *Microphysics of Clouds and Precipitation*,  
688 *Atmospheric and Oceanographic Sciences Library, vol. 18*, Springer, 237–264, doi:10.1007/  
689 978-0-306-48100-0\_17.

690 Rotstajn, L. D., 1997: A physically based scheme for the treatment of stratiform clouds and  
691 precipitation in large-scale models. I: Description and evaluation of the microphysical processes.  
692 *Q. J. R. Meteorol. Soc.*, **123**, 1227–1282.

693 Rotstajn, L. D., B. F. Ryan, and J. J. Katzfey, 2000: A scheme for calculation of the liquid fraction  
694 in mixed-phase clouds in large-scale models. *Mon. Wea. Rev.*, **128**, 1070–1088.

695 Senior, C. A., and J. F. B. Mitchell, 1993: Carbon dioxide and climate: The impact of cloud  
696 parameterization. *J. Climate*, **6**, 393–418, doi:10.1175/1520-0442(1993)006<0393:CDACTI>  
697 2.0.CO;2.

698 Sherwood, S. C., and Coauthors, 2020: An assessment of Earth’s climate sensitivity using multiple  
699 lines of evidence. *Reviews of Geophysics*, **58**, e2019RG000678, doi:10.1029/2019RG000678.

700 Soden, B. J., and G. A. Vecchi, 2011: The vertical distribution of cloud feedback in coupled  
 701 ocean-atmosphere models. *Geophys. Res. Lett.*, **38**, L12 704, doi:10.1029/2011GL047632.

702 Somerville, R. C. J., and L. A. Remer, 1984: Cloud optical thickness feedbacks in the CO<sub>2</sub> climate  
 703 problems. *J. Geophys. Res. Atmos.*, **89**, 9668–9672, doi:10.1029/JD089iD06p09668.

704 Stephens, G. L., 1978: Radiation profiles in extended water clouds. II. Parameterization schemes.  
 705 *J. Atmos. Sci.*, **35**, 2123–2132, doi:10.1175/1520-0469(1978)035<2123:RPIEWC>2.0.CO;2.

706 Storelvmo, T., I. Tan, and A. V. Korolev, 2015: Cloud phase changes induced by CO<sub>2</sub> warming—a  
 707 powerful yet poorly constrained cloud-climate feedback. *Curr. Clim. Change Rep.*, **1**, 288–296,  
 708 doi:10.1007/s40641-015-0026-2.

709 Tan, I., L. Oreopoulos, and N. Cho, 2019: The role of thermodynamic phase shifts in cloud  
 710 optical depth variations with temperature. *Geophys. Res. Lett.*, **46**, 4502–4511, doi:10.1029/  
 711 2018GL081590.

712 Tan, I., and T. Storelvmo, 2016: Sensitivity study on the influence of cloud microphysical pa-  
 713 rameters on mixed-phase cloud thermodynamic phase partitioning in CAM5. *J. Atmos. Sci.*, **73**,  
 714 709–728, doi:10.1175/JAS-D-15-0152.1.

715 Tan, I., and T. Storelvmo, 2019: Evidence of strong contributions from mixed-phase clouds to  
 716 Arctic climate change. *Geophys. Res. Lett.*, **46**, 2894–2902, doi:10.1029/2018GL081871.

717 Tan, I., T. Storelvmo, and M. D. Zelinka, 2016: Observational constraints on mixed-phase clouds  
 718 imply higher climate sensitivity. *Science*, **352**, 224–227, doi:10.1126/science.aad5300.

719 Tan, I., T. Storelvmo, and M. D. Zelinka, 2018: The climatic impact of thermodynamic phase  
 720 partitioning in mixed-phase clouds. *Mixed-Phase Clouds: Observations and Modeling*, C. An-  
 721 dronache, Ed., Elsevier, 237–264, doi:10.1016/B978-0-12-810549-8.00010-6.

722 Terai, C., R. Y. Zhang, S. A. Klein, M. D. Zelinka, J. C. Chiu, and Q. Min, 2019: Mechanisms  
 723 behind the extratropical stratiform low-cloud optical depth response to temperature in ARM site  
 724 observations. *J. Geophys. Res. Atmos.*, **124**, 2127–2147, doi:10.1029/2018JD029359.

725 Terai, C. R., S. A. Klein, and M. D. Zelinka, 2016: Constraining the low-cloud optical depth  
 726 feedback at middle and high latitudes using satellite observations. *J. Geophys. Res. Atmos.*, **121**,  
 727 9696–9716, doi:10.1002/2016JD025233.

728 Tselioudis, G. W., B. Rossow, and D. Rind, 1992: Global patterns of cloud optical thickness  
 729 variation with temperature. *J. Climate*, **5**, doi:0.1175/1520-0442(1992)005<1484:GPOCOT>2.  
 730 0.CO;2.

731 Vial, J., J.-L. Dufresne, and S. Bony, 2013: On the interpretation of inter-model spread in CMIP5  
 732 climate sensitivity estimates. *Climate Dyn.*, **41**, 3339–3362, doi:10.1007/s00382-013-1725-9.

733 Wall, C. J., and D. L. Hartmann, 2015: On the influence of poleward jet shift on shortwave cloud  
 734 feedback in global climate models. *J. Adv. Model. Earth Syst.*, **7**, doi:10.1002/2015MS000520.

735 Zelinka, M. D., T. A. Myers, D. T. McCoy, S. Po-Chedley, P. M. Caldwell, P. Ceppi, S. A. Klein,  
 736 and K. E. Taylor, 2020: Causes of higher climate sensitivity in CMIP6 models. *Geophys. Res.*  
 737 *Lett.*, **47**, e2019GL085782, doi:10.1029/2019GL085782.

738 Zelinka, M. D., C. Zhou, and S. A. Klein, 2016: Insights from a refined decomposition of cloud  
 739 feedbacks. *Geophys. Res. Lett.*, **43**, 9259–9269, doi:10.1002/2016GL069917.

740 Zhao, M., 2014: An investigation of the connections among convection, clouds, and climate  
 741 sensitivity in a global climate model. *J. Climate*, **27**, 1845–1862, doi:10.1175/JCLI-D-13-00145.  
 742 1.

743	<b>LIST OF TABLES</b>	
744	<b>Table 1.</b> Description of the experiments. . . . .	36
745	<b>Table 2.</b> Normalized changes in LWP and IWP ( $\text{g m}^{-2} \text{ K}^{-1}$ ) in the process-level exper-	
746	iments. The normalized fractional changes ( $\% \text{ K}^{-1}$ ) are in parentheses. The	
747	climatological values ( $\text{g m}^{-2}$ ) in Ctrl are also given. . . . .	37

TABLE 1. Description of the experiments.

Name(s)	Perturbation(s)
Ctrl	the control with $RH_c = 83.3\%$
Tse2K	2-K warming applied to the temperature seen by the (stratiform) cloud scheme and surface evaporation
	Process-level Experiments (Section 3a)
Qse2K	2-K warming applied to calculation of $q_s$ for the cloud scheme and surface evaporation
MI2K	2-K warming applied to <i>microphysical</i> processes: BF process, melting, homogeneous freezing, and initial phase partitioning
BF2K	2-K warming applied to the <i>BF</i> process
ME2K	2-K warming applied to <i>melting</i>
	Perturbed Parameter Experiments (Section 3b)
{quar, halv, doub, quad}BF	the BF conversion rate multiplied by {0.25, 0.5, 2, 4}
rh{767, 800, 867, 900}	$RH_c = \{76.7\%, 80\%, 86.7\%, 90\%\}$
v{050, 075, 125, 150}	the ice fall speed multiplied by {0.5, 0.75, 1.25, 1.5}
{name}_Tse2K	the corresponding Tse2K experiment for {name} (e.g., quarBF_Tse2K)

748 TABLE 2. Normalized changes in LWP and IWP ( $\text{g m}^{-2} \text{K}^{-1}$ ) in the process-level experiments. The normalized  
749 fractional changes ( $\% \text{K}^{-1}$ ) are in parentheses. The climatological values ( $\text{g m}^{-2}$ ) in Ctrl are also given.

	Extratropics		Mid-Latitudes		High-Latitudes	
	LWP	IWP	LWP	IWP	LWP	IWP
Ctrl	29.9	35.6	38.3	42.7	4.6	14.1
Tse2K	3.0 (9.9)	0.9 (2.4)	3.6 (9.3)	0.8 (1.9)	1.1 (24.2)	1.0 (7.2)
Qse2K	0.5 (1.7)	2.4 (6.8)	0.6 (1.6)	2.8 (6.7)	0.2 (5.2)	1.1 (7.9)
MI2K	2.2 (7.4)	-1.4 (-4.0)	2.6 (6.9)	-1.9 (-4.4)	0.9 (19.4)	0.0 (-0.3)
BF2K	1.7 (5.5)	-0.1 (-0.2)	1.9 (5.0)	-0.1 (-0.2)	0.9 (18.7)	0.0 (0.2)
ME2K	0.6 (2.1)	-1.4 (-3.9)	0.8 (2.1)	-1.8 (-4.2)	0.0 (0.8)	-0.1 (-0.5)

## LIST OF FIGURES

750	<b>LIST OF FIGURES</b>	
751	<b>Fig. 1.</b> Schematic of tracers and processes in the cloud microphysics scheme. Quantities in rectangles are prognostic tracers, and those in ovals are diagnostic variables.	39
752		
753	<b>Fig. 2.</b> Zonal-mean LWP and IWP ( $\text{g m}^{-2}$ ) in Ctrl and Tse2K experiments, averaged between hemispheres as for all following figures.	40
754		
755	<b>Fig. 3.</b> Normalized changes in the zonal-mean extratropical LWP (the upper panels) and IWP (the lower panels) ( $\text{g m}^{-2} \text{K}^{-1}$ ) in the process-level experiments.	41
756		
757	<b>Fig. 4.</b> Vertical distributions of the normalized changes in the zonal-mean mixing ratios of cloud liquid and ice ( $10^{-6} \text{ kg kg}^{-1} \text{K}^{-1}$ ) in the key process-level experiments. Differences between the perturbation and Ctrl runs are shown as colored shading. Ctrl run values are depicted by the contours with a spacing of $5 \cdot 10^{-6} \text{ kg kg}^{-1}$ . Thick grey lines show the $0^\circ\text{C}$ and $-40^\circ\text{C}$ isotherms. The x- and y-axes are latitude and pressure (hPa), respectively.	42
758		
759		
760		
761		
762	<b>Fig. 5.</b> Vertical distributions of the normalized changes in the zonal-mean time tendency terms of cloud liquid mixing ratio ( $10^{-9} \text{ kg kg}^{-1} \text{s}^{-1} \text{K}^{-1}$ ) in the key process-level experiments. Differences between the perturbation and Ctrl runs are shown as colored shading where a positive value indicates an increase in cloud liquid tendency. Ctrl run values are represented by the contours with a spacing of $1 \cdot 10^{-9} \text{ kg kg}^{-1} \text{s}^{-1}$ . The tendency terms shown are condensation, autoconversion, accretion, the BF process, and riming. Thick grey lines are the $0^\circ\text{C}$ and $-40^\circ\text{C}$ isotherms. The x- and y-axes are latitude and pressure (hPa), respectively.	43
763		
764		
765		
766		
767		
768		
769	<b>Fig. 6.</b> As Fig. 5, but for cloud ice instead of cloud liquid, with tendency terms shown being the BF process, riming, and gravitational ice settling.	44
770		
771	<b>Fig. 7.</b> Summary of the three main processes (highlighted by Qse2K, BF2K, and ME2K experiments) underlying the LWP/IWP feedback. Arrow width and direction represent the relative magnitude and sign (upward denoting an increase) of the extratropical LWP/IWP changes, respectively.	45
772		
773		
774		
775	<b>Fig. 8.</b> Climatological extratropical LWP ( $\text{g m}^{-2}$ ) plotted against the climatological extratropical IWP ( $\text{g m}^{-2}$ ) in the perturbed parameter experiments.	46
776		
777	<b>Fig. 9.</b> Normalized changes in extratropical LWP/IWP ( $\text{g m}^{-2} \text{K}^{-1}$ ) in the full warming (Tse2K) experiments plotted against the climatological extratropical LWP/IWP ( $\text{g m}^{-2}$ ) in the perturbed parameter experiments. Panels (a) and (b) are for LWP and IWP, respectively. The rectangle in Panel (b) is a blowup of the data points clustered around Ctrl.	47
778		
779		
780		
781	<b>Fig. 10.</b> Normalized changes in extratropical LWP ( $\text{g m}^{-2} \text{K}^{-1}$ ) in the full warming (Tse2K) experiments plotted against the climatological extratropical T5050 in the perturbed parameter experiments. The black and orange dotted lines represent the best linear fits without and with the ice fall speed experiments, respectively.	48
782		
783		
784		

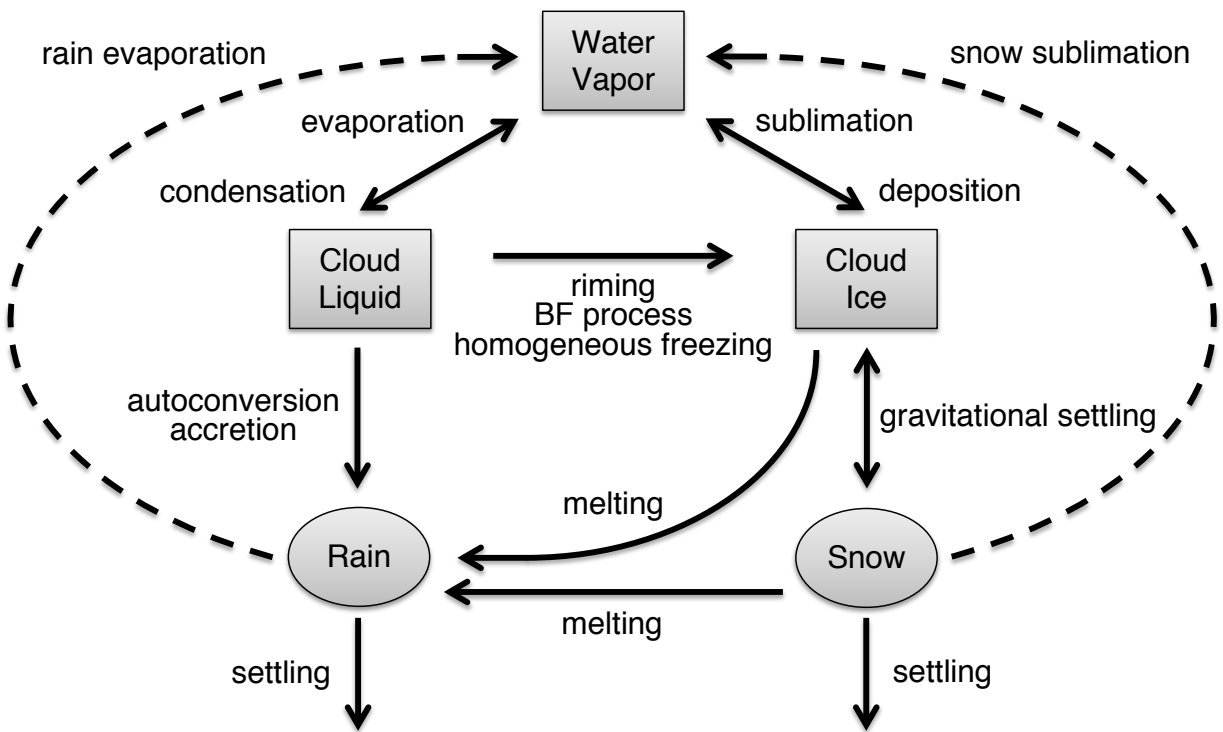
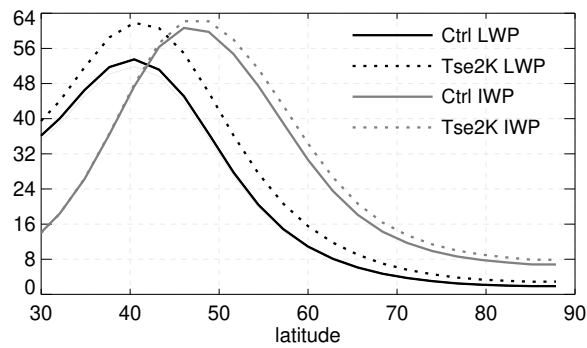


FIG. 1. Schematic of tracers and processes in the cloud microphysics scheme. Quantities in rectangles are prognostic tracers, and those in ovals are diagnostic variables.





787 FIG. 2. Zonal-mean LWP and IWP ( $\text{g m}^{-2}$ ) in Ctrl and Tse2K experiments, averaged between hemispheres as  
 788 for all following figures.

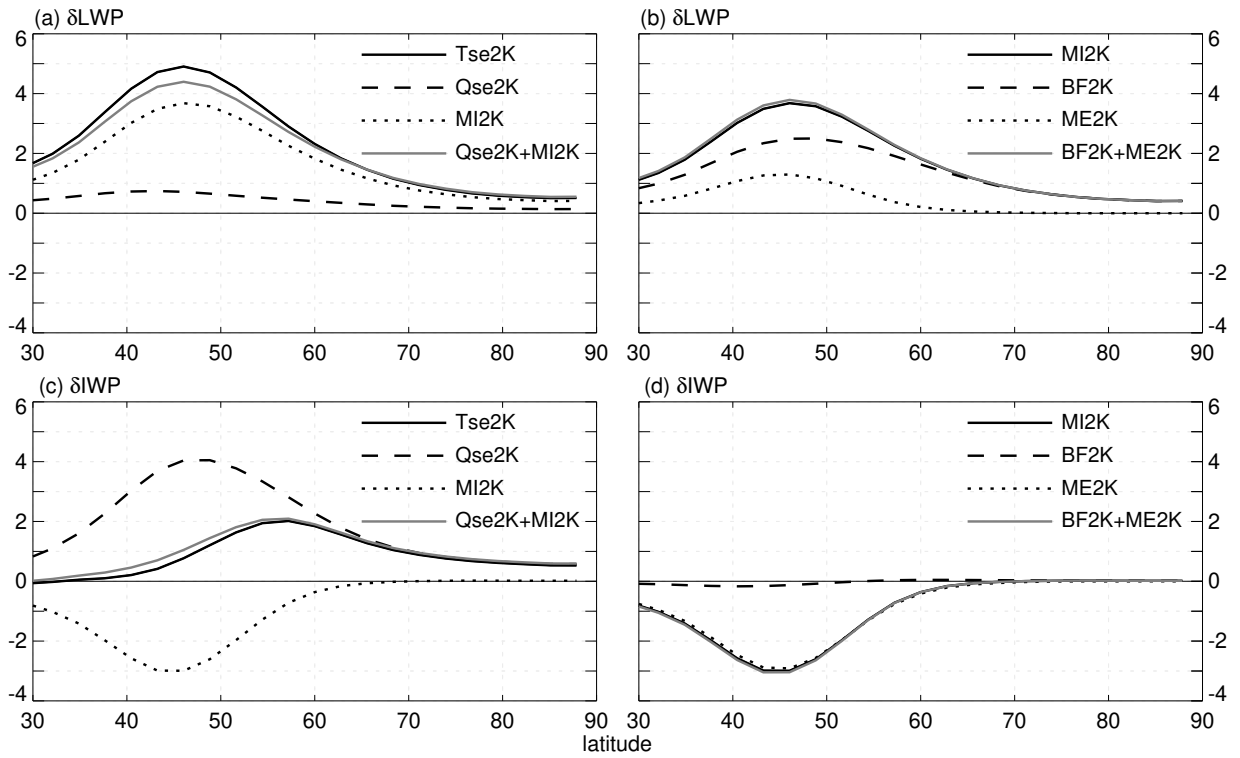
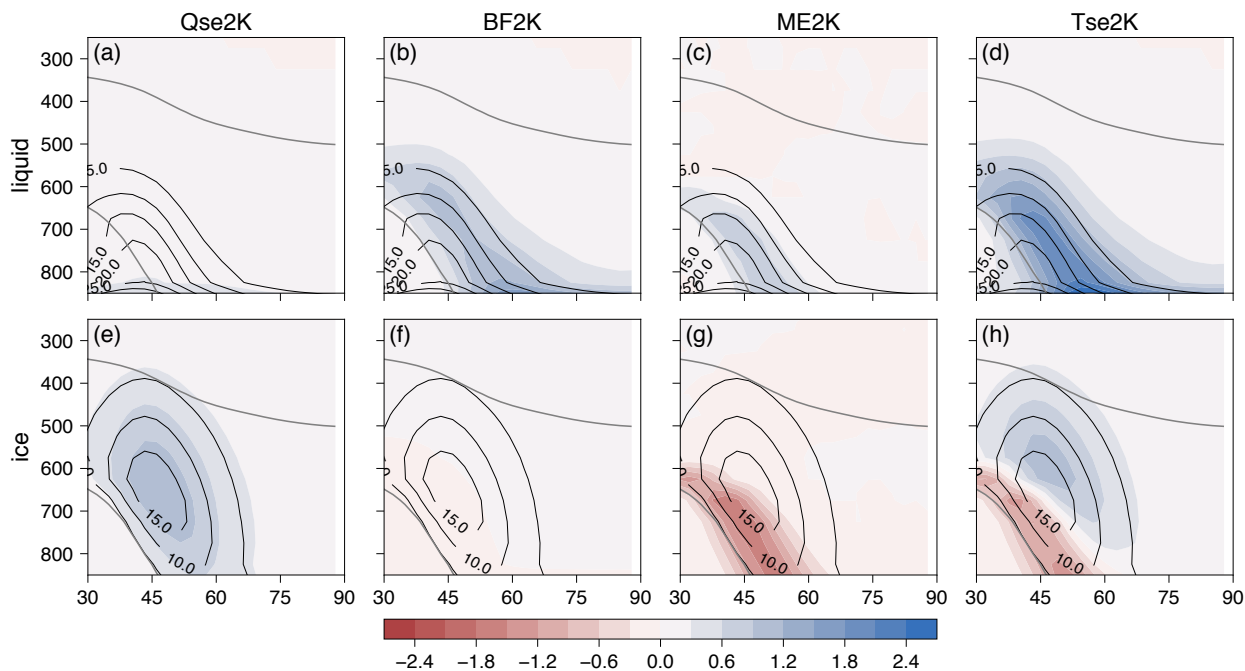


FIG. 3. Normalized changes in the zonal-mean extratropical LWP (the upper panels) and IWP (the lower panels) ( $\text{g m}^{-2} \text{K}^{-1}$ ) in the process-level experiments.



791 FIG. 4. Vertical distributions of the normalized changes in the zonal-mean mixing ratios of cloud liquid and ice  
 792 ( $10^{-6} \text{ kg kg}^{-1} \text{ K}^{-1}$ ) in the key process-level experiments. Differences between the perturbation and Ctrl runs are  
 793 shown as colored shading. Ctrl run values are depicted by the contours with a spacing of  $5 \cdot 10^{-6} \text{ kg kg}^{-1}$ . Thick  
 794 grey lines show the  $0^{\circ}\text{C}$  and  $-40^{\circ}\text{C}$  isotherms. The x- and y-axes are latitude and pressure (hPa), respectively.

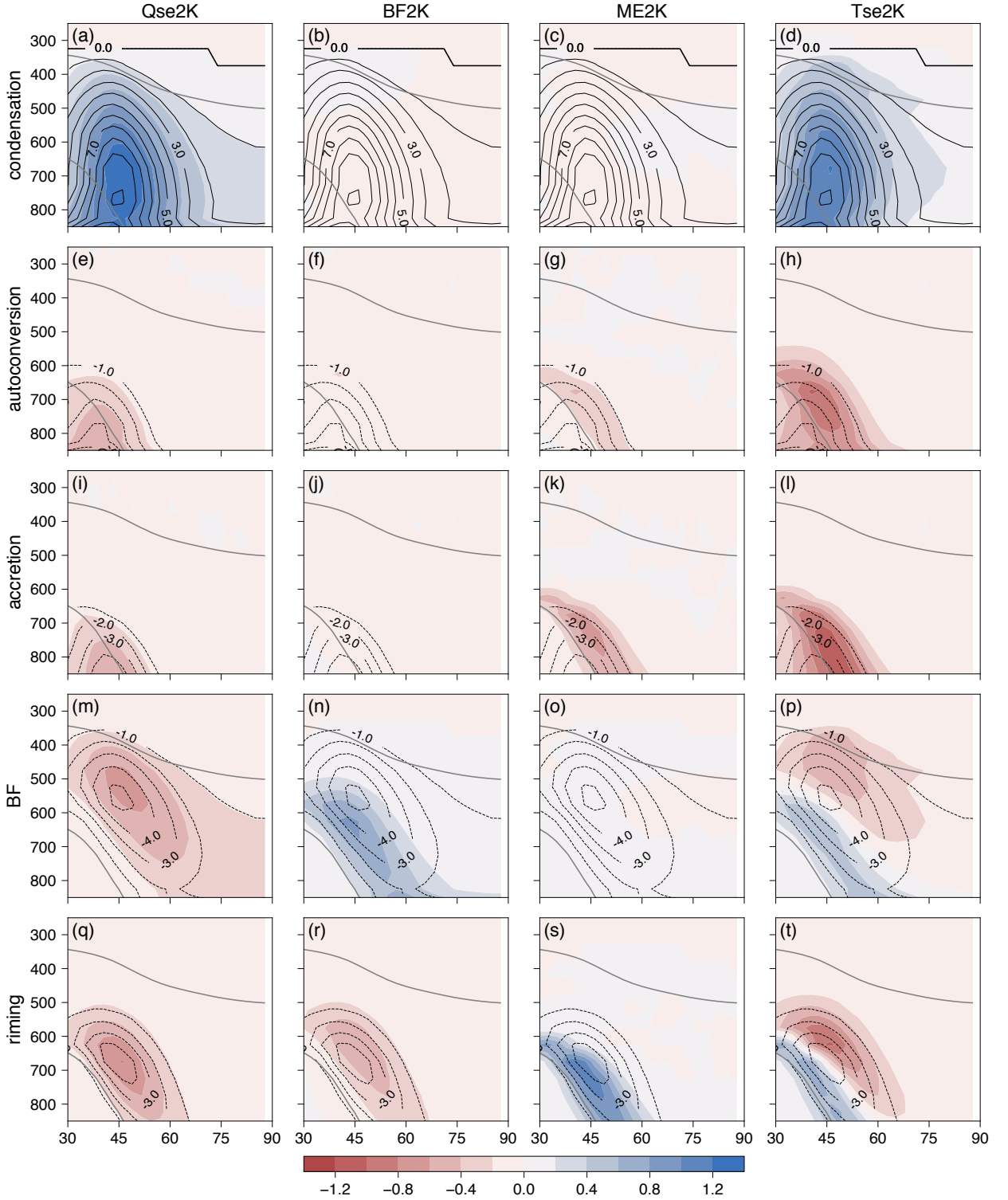


FIG. 5. Vertical distributions of the normalized changes in the zonal-mean time tendency terms of cloud liquid mixing ratio ( $10^{-9} \text{ kg kg}^{-1} \text{ s}^{-1} \text{ K}^{-1}$ ) in the key process-level experiments. Differences between the perturbation and Ctrl runs are shown as colored shading where a positive value indicates an increase in cloud liquid tendency. Ctrl run values are represented by the contours with a spacing of  $1 \times 10^{-9} \text{ kg kg}^{-1} \text{ s}^{-1}$ . The tendency terms shown are condensation, autoconversion, accretion, the BF process, and riming. Thick grey lines are the  $0^\circ\text{C}$  and  $-40^\circ\text{C}$  isotherms. The x- and y-axes are latitude and pressure (hPa), respectively.

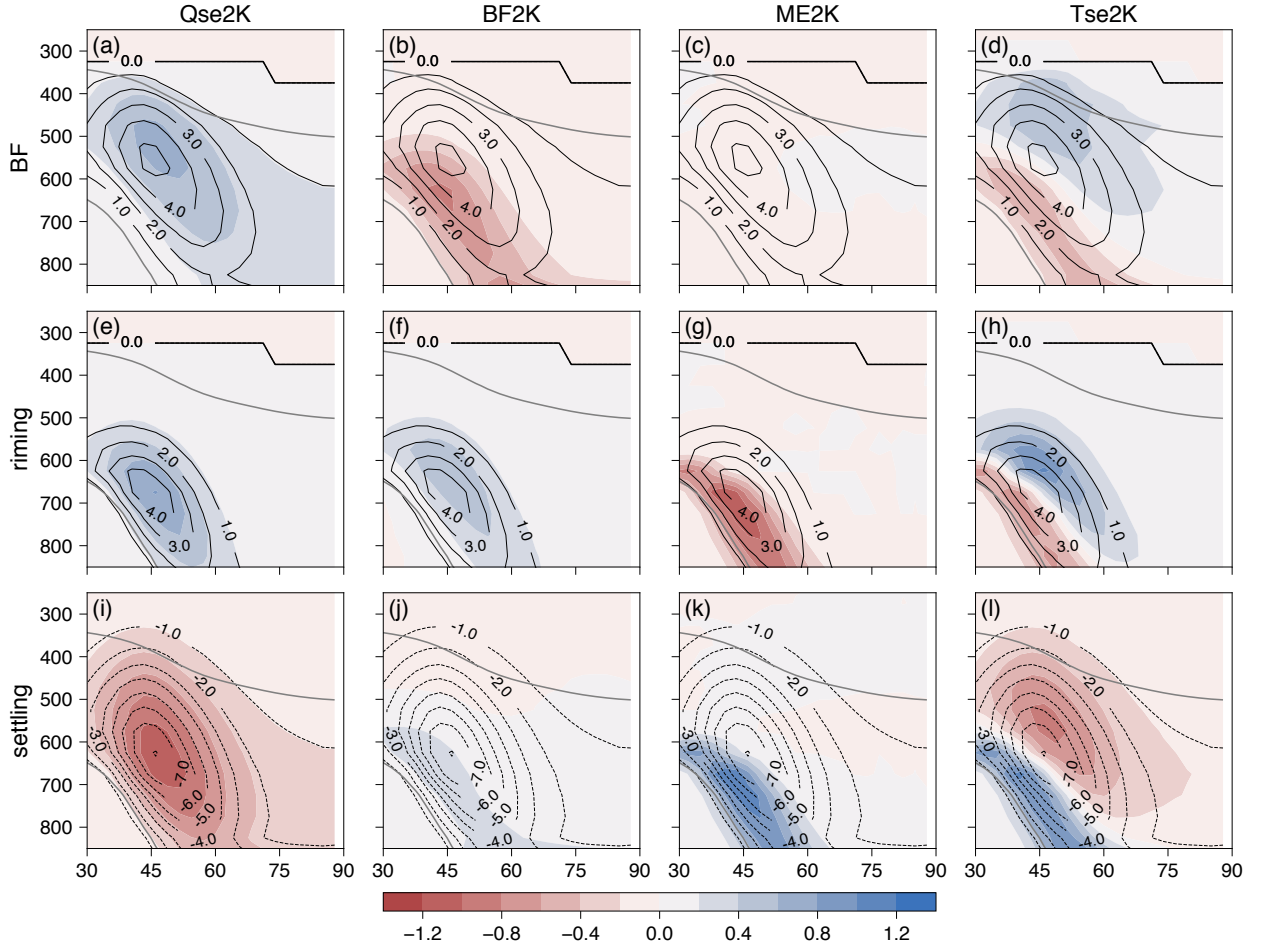


FIG. 6. As Fig. 5, but for cloud ice instead of cloud liquid, with tendency terms shown being the BF process, riming, and gravitational ice settling.

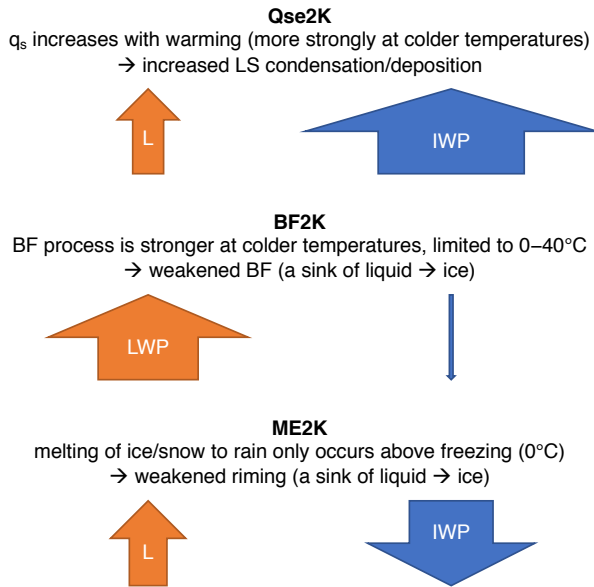


FIG. 7. Summary of the three main processes (highlighted by Qse2K, BF2K, and ME2K experiments) underlying the LWP/IWP feedback. Arrow width and direction represent the relative magnitude and sign (upward denoting an increase) of the extratropical LWP/IWP changes, respectively.

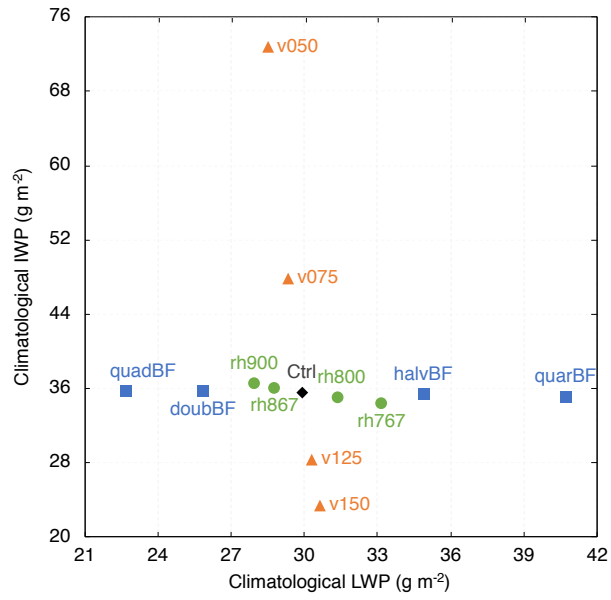


FIG. 8. Climatological extratropical LWP (g m<sup>-2</sup>) plotted against the climatological extratropical IWP (g m<sup>-2</sup>) in the perturbed parameter experiments.

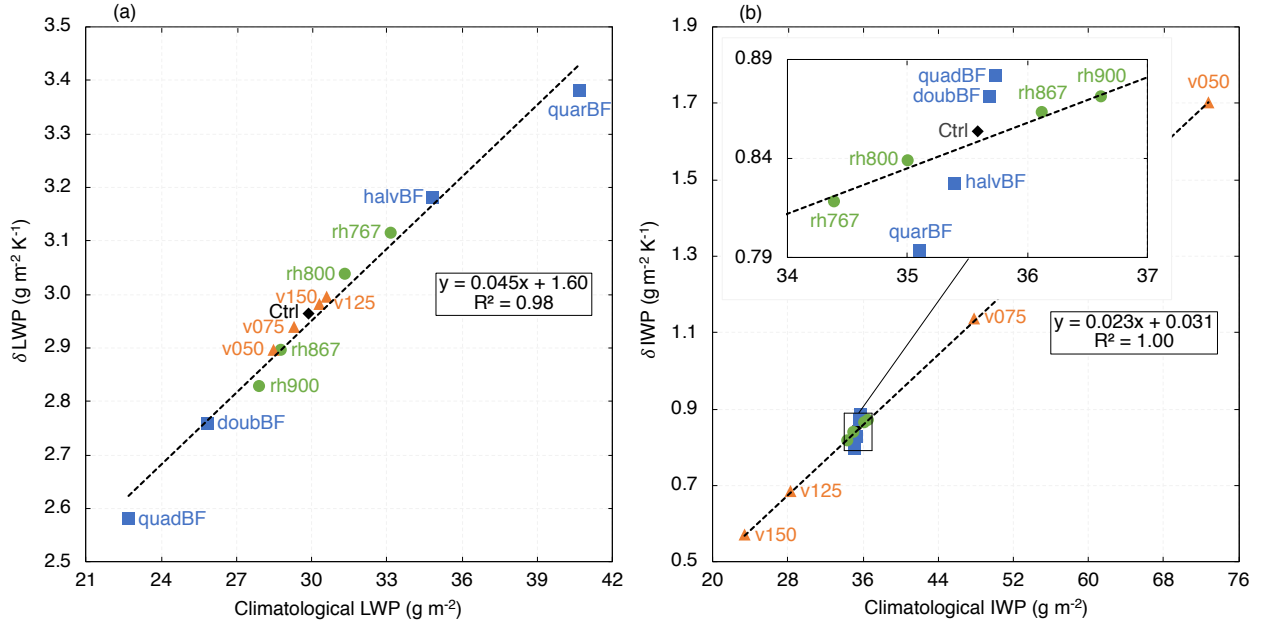


FIG. 9. Normalized changes in extratropical LWP/IWP ( $\text{g m}^{-2} \text{K}^{-1}$ ) in the full warming (Tse2K) experiments plotted against the climatological extratropical LWP/IWP ( $\text{g m}^{-2}$ ) in the perturbed parameter experiments. Panels (a) and (b) are for LWP and IWP, respectively. The rectangle in Panel (b) is a blowup of the data points clustered around Ctrl.



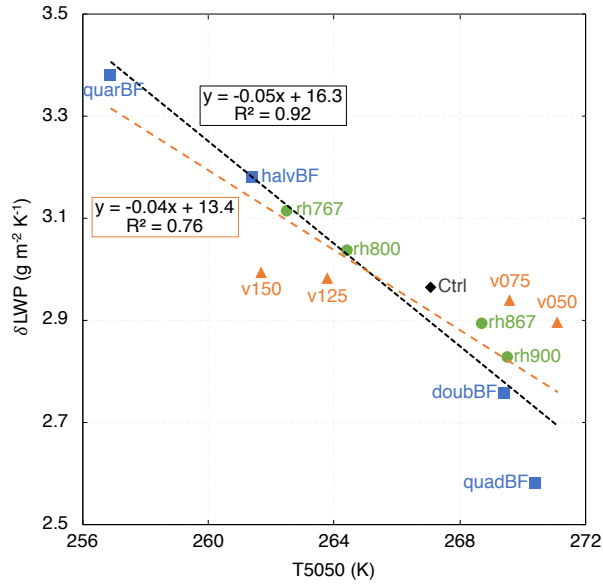


FIG. 10. Normalized changes in extratropical LWP ( $\text{g m}^{-2} \text{K}^{-1}$ ) in the full warming (Tse2K) experiments plotted against the climatological extratropical T5050 in the perturbed parameter experiments. The black and orange dotted lines represent the best linear fits without and with the ice fall speed experiments, respectively.